



Numerical and Experimental Study of the Fume Chemical Composition in Gas Metal Arc Welding

V. I. Vishnyakov¹ · S. A. Kiro¹ · M. V. Oprya¹ · O. D. Chursina¹ · A. A. Ennan¹

Received: 22 March 2018 / Revised: 26 April 2018 / Accepted: 27 April 2018 / Published online: 14 June 2018
© Institute of Earth Environment, Chinese Academy Sciences 2018

Abstract

Primary particles' sizes and chemical composition during gas metal arc welding are studied by the welding fume evolution numerical modeling. The inhalable particles' chemical composition and specific surface area are studied experimentally. The dependencies of both the particles' sizes and chemical composition on the vapor–gas mixture cooling rate are demonstrated.

Keywords Gas metal arc welding · Numerical modeling · Particle sizes · Chemical composition

List of Symbols

d	Particle diameter
e	Electron charge
E	Energy
E_s	Surface electric field
f_N	Size distribution
g	Component mass fraction
G	Gibbs free energy
I	Ionization potential
j_{ph}	Photon flux
k_B	Boltzmann constant
K_S	Saha constant
m_a	Mass of condensable atoms
$M()$	Moment of size distribution
n	Number density
N	Number of atoms in particle
P	Pressure
r	Spherical coordinate, radius
r_D	Screening length
S	Supersaturation
T	Temperature
v_T	Thermal velocity
V_b	Potential barrier
W	Work function
X	Component fraction
z	Particle charge

β	Collision kernel
φ	Electric potential
γ	Surface free energy
μ	Molecular mass
ν_e	effective electron state density
ρ	Density of matter
τ	Time scale
σ	Standard deviation
Σ	Statistical weight

1 Introduction

Arc welding usage is accompanied by emission of the welding materials' vapors. The high-temperature (~ 3000 K) vapors are ionized via electron-atom collisions and UV-radiation from arc. Ionized vapors mix with shielding gas and create the divergent flow into environmental air, which cools down with condensation of vapors into liquid droplets, named as the nuclei. The heterogeneous ion-induced nucleation takes place, because vapors are ionized. It is the beginning of the welding fumes formation.

After nucleus growth via material condensation and coalescence, these droplets are solidified and form the solid primary particles of the welding fume. Primary particles' agglomeration forms the inhalable particles in the breathing zone. All processes occur in already ionized gas, i.e., in the plasma.

Many authors study the nucleation in the plasma by numerical simulation, for example: Denysenko and Azarenkov (2011), Girshick and Warthesen (2006) and Shigeta et al. (2004). Numerical simulation allows studying the

✉ V. I. Vishnyakov
eksvar@ukr.net

¹ Physical-Chemical Institute for Environment and Human Protection of Min Edu Sci and Natl Acad Sci Ukraine, 3 Preobrazhenska st., Odessa, UA 65082, Ukraine

behavior of process depending on environmental parameters and initial conditions (Murphy et al. 2009; Schnick et al. 2010). It allows to find out what processes determine the fume formation rate (Sanibondi 2015; Tashiro et al. 2013), also morphology and chemical composition of the welding fume particles (Bogaerts et al. 2011; Carpenter et al. 2008).

The particles' sizes, their specific surface area and their chemical composition are the most important parameters of welding fumes toxicity. Moreover, the particle chemical composition as a function of particle's size must be examined because it provides insight into the physical phenomena governing formation of welding fumes.

The presented paper is devoted to numerical modeling of the primary particles' formation when gas metal arc welding (GMAW) is used. The modeling purpose is the studying of the welding fume particles' chemical composition. Chemical composition of inhalable particles and their specific surface area also are studied experimentally.

2 Description of the Ionized Environment

At the shielded metal arc welding (SMAW) the additional agents of potassium with low ionization potential (for potassium $I_K = 4.3$ eV.) are inserted into the plasma from electrode cover, and they determine the plasma ionization. The welding fumes obtained from GMAW does not contain the alkali additional agent. The condensable atoms are the source of ions. The rate of condensable atoms' thermal ionization is more weakly than in alkali metals case, because the ionization potential is higher (for iron $I_{Fe} = 7.9$ eV).

The high-temperature metal vapors from the weld materials mix up with shielding gas under the welding torch nozzle. The number density of the j th component ionizable atoms is (Vishnyakov et al. 2017b)

$$n_{Aj} = \frac{P}{k_B T} \frac{g_{j0}}{\mu_j} \left[\sum \frac{g_{j0}}{\mu_j} + \frac{1}{\mu_{sg}} \frac{T_0 - T}{T - T_{sg}} \right]^{-1}, \quad (1)$$

where P is the atmospheric pressure; g_{0j} is the initial j th component mass fraction in vapors (it is determined by the content of weld material components); μ_j is the j th component molecular mass; μ_{sg} is the shielding gas molecular mass (CO_2 in the system under consideration); T_0 is the initial vapor temperature; T_{sg} is the shielding gas temperature. The current temperature is described as

$$T = T_{sg} + (T_0 - T_{sg}) \exp \frac{-t}{\tau}, \quad (2)$$

where τ is the mixing time scale, which is defined by the materials' evaporation from welding wire and molten pool, and mechanism of vapor and shielding gas mixing

(Villiermaux and Rehab 2000). In the system under consideration $\tau = 1.7$ ms.

The equilibrium number densities of the j th component ions is obtained from Saha equation (Vishnyakov et al. 2017a):

$$n_{ij} = \frac{K_{Sj}}{2} \left(\sqrt{1 + 4 \frac{n_{Aj}}{K_{Sj}}} - 1 \right), \quad (3)$$

where K_{Sj} is the Saha constant for j th component:

$$K_S = \frac{\sum_i v_e \exp \frac{-I}{k_B T} + \frac{\pi r_a^2 j_{ph}}{k_{ei}}}{\sum_a},$$

\sum_i and \sum_a are the statistical weights of ions and atoms respectively; $v_e = 2(m_e k_B T / 2\pi \hbar^2)^{3/2}$ is the effective density of the electron states; r_a is the atom radius; $j_{ph} \sim 10^{16} \text{cm}^{-2} \text{s}^{-1}$ is the flux of photons with energy more than ionization potential; $k_{ei} \sim 10^{-6} \text{cm}^3 \text{s}^{-1}$ is the electron–ion recombination coefficient.

Equations (1)–(3) allow calculating the evolutions of component equilibrium ion number densities, which are presented in Fig. 1. The initial mass fractions are determined by the welding wire (ER 70S-6) composition: $g_{Fe} = 96.5\%$ for iron; $g_{Mn} = 2\%$ for manganese; $g_{Si} = 1\%$ for silicon; $g_{Cu} = 0.5\%$ for copper. The total equilibrium ion number density is the sum $n_i = \sum n_{ij}$.

The nuclei as the liquid particles appear in the welding fume after nucleation. Such a system should be considered as a dusty plasma, i.e., the plasma, which contains the solid or liquid particles as a dust component (Goree 1994; Fortov et al. 2004). The interphase interaction leads to the particle charging. The surface of charged particle is the additional channel for gas atoms' ionization. Therefore, there is ionization balance displacement in the space charge region (SCR) around the particle (Vishnyakov 2005, 2006).

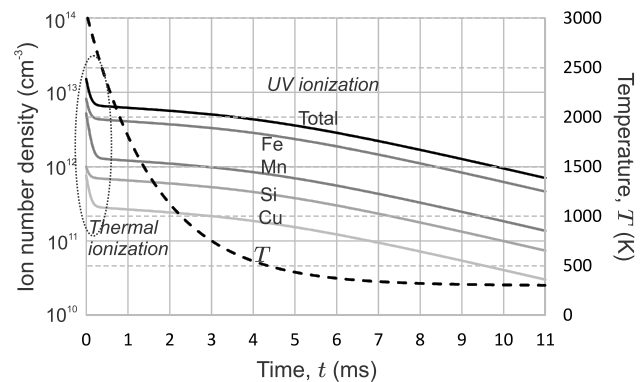


Fig. 1 Evolutions of the vapor–gas mixture temperature and equilibrium ion number densities when GMAW is used.

Electrical neutrality in this case is described by expression

$$n_e - n_i = z_p n_p, \tag{4}$$

where n_p is the particle average number density; z_p is their average charge number (a charge in the elementary charges), which can be defined from Gauss theorem for particle with radius r_p : $E_s = ez_p/r_p^2$, and potential φ distribution (Vishnyakov et al. 2017a)

$$\tanh \frac{r_p e \varphi(r)}{r_D k_B T} = \tanh \frac{r_p V_b}{r_D k_B T} \cdot \frac{r_p}{r} \exp \frac{r_p - r}{r_D},$$

from which follows

$$E_s = \frac{k_B T r_D}{2er_p^2} \sinh \frac{2r_p V_b}{r_D k_B T},$$

and, accordingly,

$$z_p = \frac{k_B T r_D}{2e^2} \sinh \frac{2r_p V_b}{r_D k_B T}, \tag{5}$$

where $r_D = \sqrt{k_B T / 8\pi e^2 n_0}$ is the screening length ($r_D \sim 1 \mu\text{m}$ in the system under consideration) and V_b is the potential barrier on the plasma-particle boundary.

Here it should be noted that nucleus has negative charge because environment is enriched by electrons, and potential barrier is:

$$V_b \cong \frac{2}{5} k_B T \ln \frac{n_{es}}{n_0} \quad (n_{es} < n_0),$$

where n_{es} is the surface electron number density:

$$n_{es} = v_e \exp \frac{-W}{k_B T} + \frac{Yj_{ph}}{v_{Te}};$$

Y is the quantum yield; $v_{Te} = \sqrt{8k_B T / \pi m_e}$ is the thermal velocity of electrons; W is the electron work function with taken into account the dependency of the work function on the particle size $W = W_0 + 0.39e^2/r_p$ (Smirnov, 1997) and W_0 is the work function for flat surface.

3 Modeling of the Nucleation and Multicomponent Condensation

The welding fume formation is the result of heterogeneous ion-induced nucleation in the environment enriched by electrons. Thus, there is an energy and charge exchange between nucleus and the environment. Such consideration has been proposed by Vishnyakov (2008) and Vishnyakov et al. (2011, 2013), where the change in Gibbs free energy as a result of nucleation is determined in the following form:

$$\Delta G = 4\pi r_n^2 \gamma - \frac{4}{3} \pi r_n^3 \frac{\rho k_B T \ln(S)}{m_a} + E_\gamma + E_{ex} + E_q, \tag{6}$$

where r_n is the nucleus radius; $\gamma = \gamma_0 r_n / (r_n + 2\delta)$ is the surface free energy of the nucleus; γ_0 is the surface free energy of the flat; δ is the Tolmen length; m_a is the mass of the condensable atoms; ρ is the nucleus density; S is the supersaturation of the condensable material.

In Eq. (6), the first two terms describe the change in Gibbs free energy defined by the classical nucleation theory (Green and Lane 1964; Reist 1984). The term E_γ is the change in surface free energy as a result of the electrical double layer on the nucleus surface formation:

$$E_\gamma = -\frac{z_n V_b}{2};$$

E_{ex} is the change in Gibbs free energy as a result of the interphase energy exchange:

$$E_{ex} = -z_n \left(W_n + \frac{3}{2} k_B T \right);$$

E_q is the change in Gibbs free energy as a result of the nucleus charging; it has a different definition for the conductor and dielectric:

$$E_{qm} = \frac{e^2}{2} \left[\frac{z_n^2}{r_n} + \frac{1}{r_n} - \frac{1}{r_i} \right] \text{-for conductor,}$$

$$E_{qd} = \frac{e^2(\epsilon - 1)}{2\epsilon} \left[\frac{6}{5} \frac{z_n^2}{(\epsilon - 1)r_n} + \frac{1}{r_n} - \frac{1}{r_i} \right] \text{-for dielectric,}$$

where z_n is the nucleus charge number; ϵ is the dielectric constant; r_i is the radius of the single-charged positive ion, which induced the nucleation.

The two kinds of nuclei are formed by the heterogeneous ion-induced nucleation: the equilibrium nuclei with radius r_{eq} , which are in the equilibrium state with the environment; and the non-equilibrium critical nuclei with radius r_{cr} , which appear as a result of fluctuations. The radius of the equilibrium nucleus is defined as a minimum of the function $\Delta G(r_n)$, and the radius of the critical nucleus is defined as a maximum of the function $\Delta G(r_n)$.

The number density of equilibrium nuclei with radius $r_n = r_{eq}$ is determined in the following form (Vishnyakov et al. 2013):

$$n_n = \frac{n_{a0}}{N_n + N_n^{-3/2} \exp \frac{\Delta G(r_{eq})}{k_B T}}, \tag{7}$$

where n_{a0} is the initial (prior to the nucleation start) condensable atom number density; N_n is the number of atoms in one nucleus: $N_n = 4\pi\rho r_n^3/3m_a$.

The nuclei number density (7) is $n_n \sim 10^{15} - 10^{16}\text{cm}^{-3}$ and much more than ion number density (3). However, the ions are the centers of ion-induced nucleation and their number should correspond to nuclei number. When nucleation occurs, ions disappear from gas phase and electron-ion recombination is replaced by the neutralization of nuclei with more great collision cross-section. As a result, the balance between ionization and recombination is broken in favor of ionization, and new electrons and ions appear in the plasma. Thus, arises a new equilibrium state for nuclei and gas phase. The time of ionization balance stabilization is $\sim 10^{-9}\text{s}$.

After nucleation of the predominant component, the fluxes of the accompanying low-boiling components on to the iron nucleus appear, because the partial pressure of these components at the nucleus surface is zero. Therefore, condensation of these components on the nucleus droplet occurs. The condensation or evaporation of the j th component is defined by density of its saturated vapor over surface of the droplet with multicomponent solution, which is described by Raoult’s law (Vishnyakov et al. 2014b). In the result, the change in the number of atoms of the j th component in the multicomponent droplet is described by the following equation:

$$\frac{dN_j}{dt} = \alpha_{cj}\pi r_n^2 v_{Tj} n_{aj} \left(1 - X_j \frac{S_{Rj}}{S_j}\right),$$

where α_{cj} is the evaporation–condensation coefficient (Okuyama and Zung, 1967) for j th component; $v_{Tj} = \sqrt{8k_B T/\pi m_{aj}}$

is the thermal velocity of the j th component atoms; m_{aj} is their mass; n_{aj} is their number density; X_j is the j th component fraction; S_j is the current j th component supersaturation; $S_{Rj} = P_{jsat}(r_n)/P_{jsat}(\infty)$ is the change in vapor partial pressure at the account of the surface curvature and inter-phase interaction, which follows from (6):

$$\ln S_R \cong \frac{m_a}{4\pi\rho k_B T} \left[8\pi\gamma_0 \frac{r_n + 3\delta}{(r_n + 2\delta)^2} - \frac{z_n(V_b + W)}{r_n^3} - \frac{e^2(1 - z_n^2)}{2r_n^4} \right]. \tag{8}$$

Then the change in the radius of nucleus droplet is

$$\frac{dr_n}{dt} = \sum_j \left[\frac{\alpha_{cj} v_{Tj} m_{aj} n_{aj}}{4\rho_j} \left(1 - X_j \frac{S_{Rj}}{S_j}\right) \right]. \tag{9}$$

At the moment of nucleation the content of the accompanying low-boiling components in the nucleus $X_{j\neq\text{Fe}} = 0$. Therefore, growth of the nucleus droplet by the deposition of these

components on the nucleus surface takes place, which determines the initial nucleus chemical composition.

The vapors’ condensation leads to decrease of their number densities. Therefore, equilibrium atom number density of the j th component in the gas phase must be reduced by number of atoms in the condensed phase, which is determined as $N_{caj} = n_n N_n X_j$.

The equilibrium nucleus is in the stable stage and some activation energy $E_{act} = \Delta G(r_{cr}) - \Delta G(r_{eq})$ is necessary for the nucleus growth via iron condensation. This activation energy decreases down to zero ($E_{act} \rightarrow 0$) with the vapor–gas mixture cooling, thus the equilibrium and the critical radii tend to equal value ($r_{eq} \rightarrow r_{cr}$). After that, the unrestricted growth of nuclei via iron condensation begins, until the condensable materials does not deplete. However, condensation of the low-boiling components are taken into account in evolutions of the particle sizes until these solidification.

4 Modeling of the Primary Particles Formation

The large number density of nuclei causes their intensive Brownian collisions and coagulation, because coagulation is accompanied by the system free energy minimization (Vishnyakov and Dragan 2003). As nuclei are in liquid state, their coagulation is a coalescence. As a result, the coagulated droplets, which grow through coalescence and condensation (9), are formed. However, it is necessary to take into account that the nucleation continues, and the system thermodynamics requires the presence of the nuclei with equilibrium number density (7). Therefore, number and size of nuclei cannot change via coalescence, because new nuclei appear. This requirement is removed after the nucleation termination.

Thus, already at the initial stage of nucleation the bimodal size distribution of the droplets occurs. The first mode contains the droplets of nuclei with radius r_n ; coagulated droplets with radius $r_{cd} > r_n$ resulting from the long-term coalescence and condensation represent the second mode. These droplets can be described by a log-normal size distribution, which is based on the number of atoms N contained in the droplets, using probability density function for two modes (Seigneur et al. 1986)

$$f_N = \frac{n_n}{N\sqrt{2\pi \ln \sigma_n}} \exp \frac{-(\ln N - \ln N_{0n})^2}{2 \ln^2 \sigma_n} + \frac{n_{cd}}{N\sqrt{2\pi \ln \sigma_{cd}}} \exp \frac{-(\ln N - \ln N_{0cd})^2}{2 \ln^2 \sigma_{cd}}, \tag{10}$$

where index n is used for nuclei, index cd is used for coagulated droplets; $N_0 = \bar{N} \exp(-\ln^2 \sigma/2)$ is the median of distribution; σ is the standard deviation; \bar{N} is the average number

of atoms in the droplets, for which the equation of the atoms conservation is as follows:

$$N_{ca} = n_n \bar{N}_n + n_{cd} \bar{N}_{cd}$$

The numerical calculation of the coagulation of particles is the complex problem. Therefore, Cohen and Vaughan (1971) proposed the approximation method based on the moments of size distribution. The moments are described by the following equation:

$$M(k) = \int_0^\infty N^k f_N dN,$$

and the Brownian coagulation can be described as (Yu et al. 2008)

$$\frac{\partial M(k)}{\partial t} = \frac{1}{2} \int_0^\infty f_N \int_0^\infty \beta(N, N') f_{N'} \times [(N + N')^k - N^k - N'^k] dN' dN, \tag{11}$$

where N and N' are the numbers of atoms in the colliding droplets; $\beta(N, N')$ is the collision kernel. If the droplets are much smaller than mean free path of the gas particles, the Brownian collision kernel should be determined by the kinetic theory of gases (Shigeta et al. 2004):

$$\beta(N, N') = \beta_0 (N^{1/3} + N'^{1/3})^2 \sqrt{\frac{N + N'}{NN'}}$$

$$\beta_0 = \left(\frac{3m_a}{4\pi\rho}\right)^{1/6} \sqrt{\frac{6k_B T}{\rho}}$$

where Coulomb interaction is neglected because $e^2 z z' / (a + a') \ll k_B T$ (a is the r_n or r_{cd} ; z is the z_n or z_{cd} , respectively).

The evolution of the moments (11) can be defined for each mode (10) (Vishnyakov et al. 2014a). The PTC Mathcad Prime program allows calculating the evolution of integral moments (11) with using the log-normal distribution theory (Pratsinis 1988), without any additional approximations. The zero moments represent the total number densities of the generated particles n_n and n_{cd} . The total numbers of atoms in these are defined by the first moments. As a result, the average number of atoms in the droplets of each mode is

$$\bar{N}_n = \frac{M_n(1)}{M_n(0)}, \quad \bar{N}_{cd} = \frac{M_{cd}(1)}{M_{cd}(0)} \tag{12}$$

and the standard deviations are defined by the following equations:

$$\ln^2 \sigma_n = \ln \frac{M_n(0)M_n(2)}{M_n(1)^2}, \quad \ln^2 \sigma_{cd} = \ln \frac{M_{cd}(0)M_{cd}(2)}{M_{cd}(1)^2}. \tag{13}$$

Equations (10)–(13) allow to describe the evolution of the coalescence in the bimodal system of droplets with taken into account both the intramodal coalescence and the intermodal association of the different droplet modes.

The droplets' growth and coalescence proceed while vapor–gas mixture cools down to solidification temperature. After solidification the agglomeration of solid primary particles begins. It should be noted that solidification temperature depends on the droplet size (Shu et al. 2012). The coagulated droplets solidify earlier than the droplets of the nuclei; and the transient stage exists when the coagulated mode is represented by solid particles, but the nucleus mode is the liquid droplets. The bimodal coalescence terminates when the coagulated droplets become solid particles. There is only coalescence of the first mode.

The calculation results are presented in Figs. (2)–(4). Evolutions of the average nuclei and coagulated droplets radii with taken into account both condensation and coagulation growths are presented in Fig. 2. Cooling of the vapor–gas mixture to the temperature of coagulated droplets solidification occurs during 0.9 ms. After that, this mode don't change by the coalescence or vapor condensation, only nuclei growth is proceeded.

The average diameter of the solid primary particles which are formed from the nuclei is $d_n = 4.3$ nm and $d_{cd} = 8.4$ nm for primary particles which are formed from the coagulated droplets. Number density of the nucleus mode primary particles is $6 \times 10^{14} \text{cm}^{-3}$ and greatly exceeds the coagulated droplet mode number density, which is $4 \times 10^{13} \text{cm}^{-3}$.

Evolutions of the chemical compositions are presented in Fig. 3 for nuclei and in Fig. 4 for coagulated droplets. The increase of the droplet size leads to change in the components' condensation intensity, as it follows from Eq. (8), that causes the change in the chemical composition.

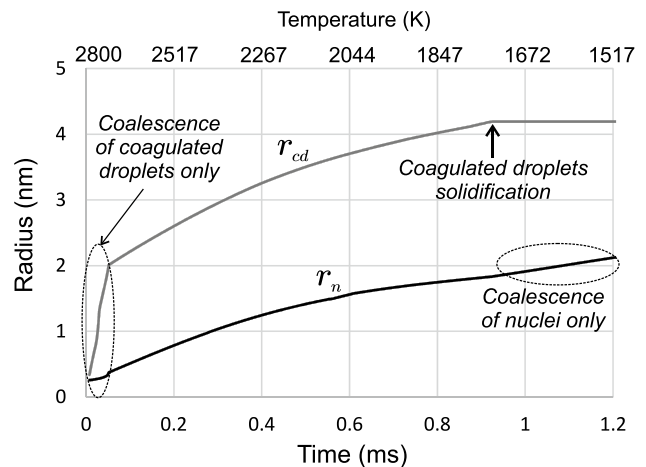


Fig. 2 Evolutions of the average nucleus r_n and coagulated droplet r_{cd} radii

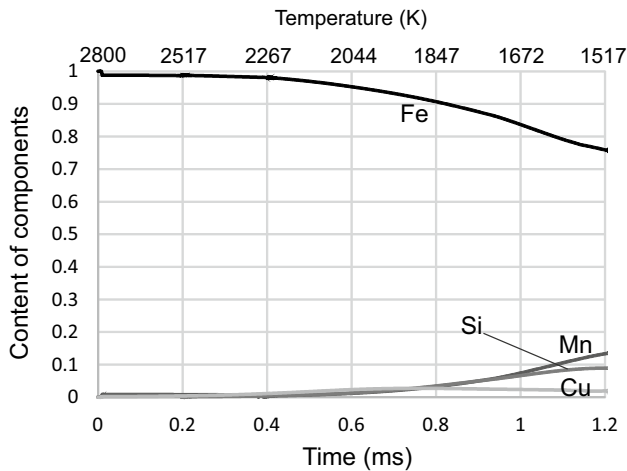


Fig. 3 Evolution of the nucleus droplet chemical composition

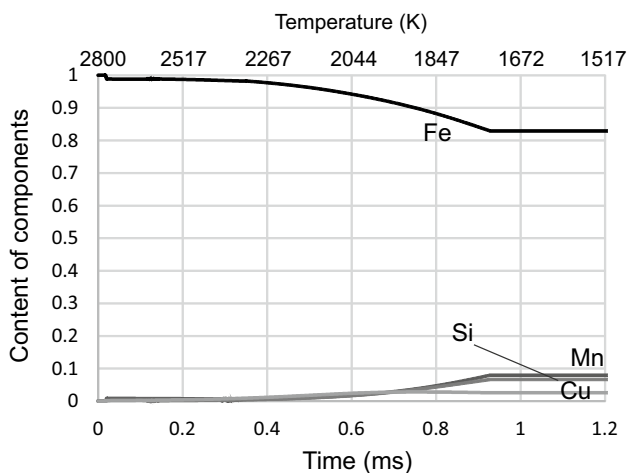


Fig. 4 Evolution of the coagulated droplet chemical composition

5 Experimental Results and Discussion

Due to the intramodal agglomeration, the differences in the primary particle modes size and chemical composition may lead to compositional and specific area inhomogeneities for different size range groups of the inhalable particles. To confirm this assumption, it is necessary to examine each size range group of the inhalable particles independently from the others.

For comparison of the computed results to experimental data, the experimental equipment, which scheme is presented in Fig. 5, was used. The power source is Paton PSI-250R inverter rectifier. The welding wire is ER 70S-6 with 0.8 mm diameter. The reverse polarity direct current is 90 ± 5 A; voltage is 21 ± 0.5 V; and wire feed speed is

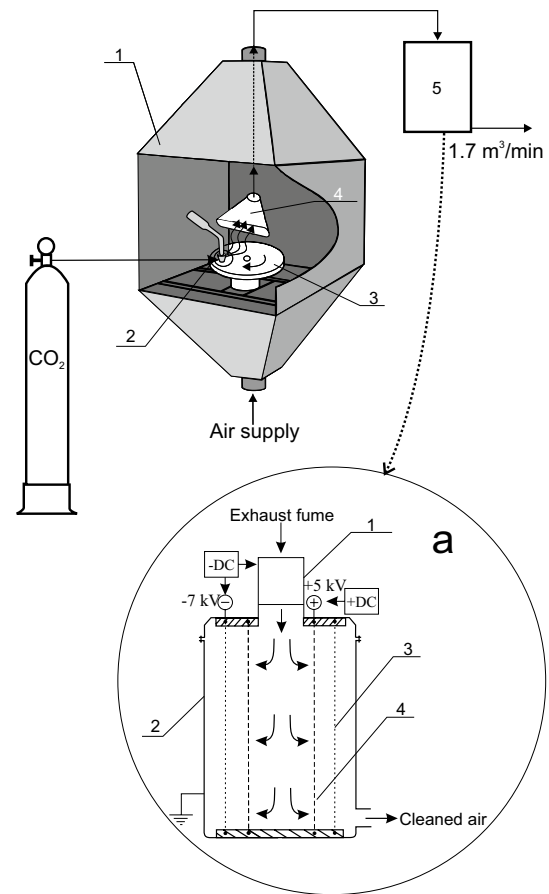


Fig. 5 Experimental equipment scheme: 1, fume chamber; 2, welding torch; 3, turntable; 4, slit air inlet; 5, electrostatic precipitator; (a) Grid-type electrostatic precipitator scheme: 1, charging section; 2, grid section; 3, fine filter; 4, coarse filter

7 ± 0.5 cm/s. At the distance of 20 cm from the arc, the welding fume was extracted with air co-flow of $1.7 \text{ m}^3/\text{min}$.

Inhalable particles are the result of the primary particles agglomeration and also are described by the bimodal size distribution (Ennan et al. 2013; Vishnyakov et al. 2014c). The first mode is presented by the agglomerates with average diameter of 180–200 nm, and the second mode—with average diameter of 250–300 nm.

The GMAW fume was separated into two fractions by the grid-type electrostatic precipitator. The precipitator consists of two sections: the grid section and the charging section, shown together in Fig. 5a. The charging section, in the form of a corona discharge ionizer (Vishnyakov et al. 2016), is located above the grid section. The voltage on the inner multi-needle discharge electrode is negative 7 kV, resulting in the total corona current of 0.6 mA with fume flowing, which provides the fume particles' negative charging.

The grid section is mounted in the filter holder assembly and consists of two metallic coaxial cylinder-type filters with

the interspace of 3 cm. The coarse filter with diameter of 14 cm is the perforated metal plate with circular holes of diameter 1.2 mm and open area 27%. The potential of coarse filter is positive 5 kV. The fine filter with diameter of 20 cm is the wire mesh with mesh opening of 0.063 mm, wire diameter of 0.04 mm and open area 37%. The potential of fine filter is negative 7 kV. The precipitator collection efficiency was about 99%, based on the welding fume mass concentration.

Welding fume particles' deposits on the upstream face of the coarse filter preferentially contain particles of the second mode, whereas the first mode particles are deposited on the fine filter and on the downstream face of the coarse filter as a result of the electric force acting on them in the direction opposing the fume flow.

After filtration, the three powder samples were analysed by a Quantachrome Autosorb-6B (Quantachrome Instruments, Boynton Beach, FL, USA) for determination of the specific surface area (A_S). The defined by BET method values are presented in Table 1. These three powder samples also were analysed by atomic absorption spectroscopy Saturn-3P1 (Optron Instrument-Making Plant, Minsk, Belarus) for determination of the chemical composition. Recalculation on the initial elements which contain in the welding wire, i.e., with exclusion of oxygen and carbon, gives the presented in Table 1 results.

There is correlation well between calculation and experimental data, i.e., the difference in the chemical composition of the primary particle modes remains in the inhalable particle modes, despite averaging over numerous primary particles that formed each agglomerate, that can be caused by great difference in the primary particle number densities of the different modes.

In the system under consideration, content of iron in the primary particles which are formed from the coagulated droplets is higher than in the primary particles from the nuclei and strongly depends on the cooling rate, which is determined by the mixing time scale τ in Eq. (2). In the case under consideration this time is $\tau = 1.7$ ms, that provides content of iron 77% in the nuclei with average diameter

$d_n = 4.3$ nm and 84% in the coagulated droplets with average diameter $d_{cd} = 8.4$ nm.

Increase of the time scale up to 3 ms provides content of iron 54% in the nuclei with average diameter $d_n = 5.8$ nm and 76% in the coagulated droplets with average diameter $d_{cd} = 10.5$ nm. The evolutions of the chemical composition for this case are presented in Figs. 6 and 7.

Thus, the vapor–gas mixture cooling rate allows to define the primary particle sizes and their chemical composition. The dependency of the particles' sizes on the cooling rate is confirmed experimentally by Vishnyakov et al. (2017b).

6 Conclusion

Evolution of the primary particles' sizes and chemical compositions in the welding fumes from GMAW was investigated via numerical modeling. The inhalable particles' chemical composition and specific surface area were studied experimentally.

The primary particles are described by the bimodal size distribution as a result of nuclei coalescence. Bimodal size

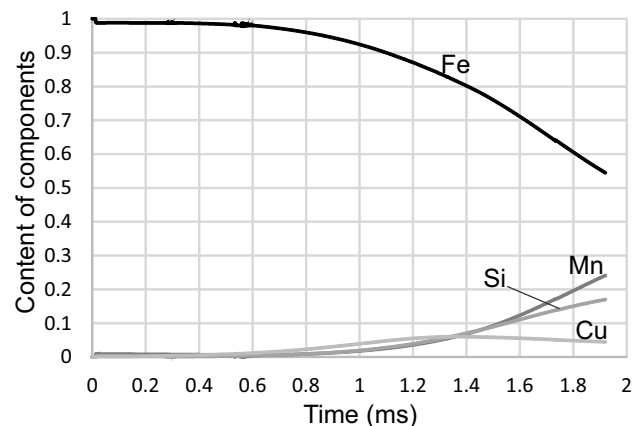


Fig. 6 Evolution of the nucleus droplet chemical composition for $\tau = 3$ ms

Table 1 Experimental data and calculation results

	Experiment			Calculation	
	Fine filter	Coarse filter: downstream	Coarse filter: upstream	Nuclei	Coagulated droplets
Mass fraction (%)	33	39	28	71	29
Specific area (m^2/g)	28.5	30.8	16.8	33	16
Content of Fe (%)	79.3	77.4	85.4	77	84
Content of Mn (%)	12.5	12.8	10.3	13	8
Content of Si (%)	7.38	9.03	3.96	9	6
Content of Cu (%)	0.82	0.77	0.34	1	2

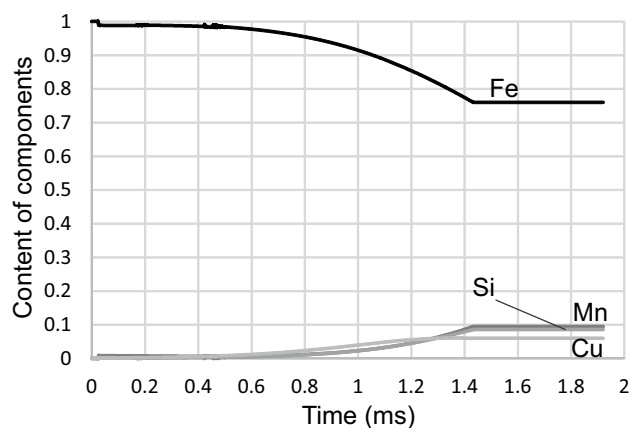


Fig. 7 Evolution of the coagulated droplet chemical composition for $\tau = 3$ ms

distribution remains for inhalable particles, which are the agglomerates of solid primary particles.

The primary particle different modes have different chemical composition, because both, the multicomponent condensation and the liquid droplets solidification depend on the particle size. The primary particle modes chemical composition and their average diameter strongly depends on the vapor–gas mixture cooling rate. This fact create the chance to regulate the chemical composition by changing the cooling rate.

The variations in element composition and specific area for different size range groups of the inhalable particles reflect the differences in the chemical composition and sizes of the primary particle modes. For assessing the harmful effects of the welding fumes, the particles should be collected with separation by sizes and each size's range group should be analyzed independently. The obtained results could be useful for sanitary-hygienic assessments of welding consumables and conditions.

References

Bogaerts A, Eckert M, Mao M, Neyts E (2011) Computer modelling of the plasma chemistry and plasma-based growth mechanisms for nanostructured materials. *J Phys D Appl Phys* 44:174030

Carpenter KR, Monaghan BJ, Norrish J (2008) Influence of shielding gas on fume size morphology and particle composition for gas metal arc welding. *Iron Steel Inst Jpn Int* 48:1570–1576

Cohen ER, Vaughan EU (1971) Approximate solution of the equations for aerosol agglomeration. *J Colloid Interface Sci* 35:612–623

Denysenko I, Azarenkov NA (2011) Formation of vertically aligned carbon nanostructures in plasmas: numerical modelling of growth and energy exchange. *J Phys D Appl Phys* 44:174031

Ennan AA, Kiro SA, Oprya MV, Vishnyakov VI (2013) Particle size distribution of welding fume and its dependency on conditions of shielded metal arc welding. *J Aerosol Sci* 64:103–110

Fortov VE, Khrapak AG, Khrapak SA, Molotkov VI, Petrov OF (2004) Dusty plasmas. *Phys Uspekhi* 47:447–492

Girshick SL, Warthesen SJ (2006) Nanoparticles and plasmas. *Pure Appl Chem* 78:1109–1116

Goree J (1994) Charging of particles in plasma. *Plasma Sour Sci Technol* 3:400–406

Green H, Lane W (1964) Particulate clouds: dusts, smokes and mists, 2nd edn. Van Nostrand, New York

Murphy AB, Tanaka M, Yamamoto K, Tashiro S, Sato T, Lowke JJ (2009) Modelling of thermal plasmas for arc welding: the role of the shielding gas properties and of metal vapour. *J Phys D Appl Phys* 42:194006

Okuyama M, Zung JT (1967) Evaporation–condensation coefficient for small droplets. *J Chem Phys* 46:1580–1585

Pratsinis SE (1988) Simultaneous nucleation, condensation and coagulation in aerosol reactors. *J Colloid Interface Sci* 124:416–427

Reist PC (1984) Introduction to aerosol science. Macmillan Publishing, New York

Sanibondi P (2015) Numerical investigation of the effects of iron oxidation reactions on the fume formation mechanism in arc welding. *J Phys D Appl Phys* 48:345202

Schnick M, Fuessel U, Hertel M, Haessler M, Spille-Kohoff A, Murphy AB (2010) Modelling of gas–metal arc welding taking into account metal vapor. *J Phys D Appl Phys* 43:434008

Seigneur C, Hudischewskyj AB, Seinfeld JH, Whitby KT, Whitby ER, Brock JR, Barnes HM (1986) Simulation of aerosol dynamics: a comparative review of mathematical models. *Aerosol Sci Technol* 5:205–222

Shigeta M, Watanabe T, Nishiyama H (2004) Numerical investigation for nano-particle synthesis in an RF inductively coupled plasma. *Thin Solid Films* 457:192–200

Shu Q, Yang Y, Zhai Y, Sun DM, Xiang HJ, Gong XG (2012) Size-dependent melting behavior of iron nanoparticles by replica exchange molecular dynamics. *Nanoscale* 4:6307–6311

Smirnov BM (1997) Processes in plasma and gases involving clusters. *Phys Uspekhi* 40:1117–1147

Tashiro S, Zeniya T, Murphy AB, Tanaka M (2013) Visualization of fume formation process in arc welding with numerical simulation. *Surf Coat Technol* 228:S301–S305

Villiermaux E, Rehab H (2000) Mixing in coaxial jets. *J Fluid Mech* 425:161–185

Vishnyakov VI (2005) Interaction of dust grains in strong collision plasmas: diffusion pressure of nonequilibrium charge carriers. *Phys Plasmas* 12:103502

Vishnyakov VI (2006) Electron and ion number densities in the space charge layer in thermal plasmas. *Phys Plasmas* 13:033507

Vishnyakov VI (2008) Homogeneous nucleation in thermal dust-electron plasmas. *Phys Rev E* 78:056406

Vishnyakov VI, Dragan GS (2003) Thermodynamic reasons of agglomeration of dust particles in the thermal dusty plasma. *Condens Matter Phys* 6:687–692

Vishnyakov VI, Kiro SA, Ennan AA (2011) Heterogeneous ion-induced nucleation in thermal dusty plasmas. *J Phys D Appl Phys* 44:215201

Vishnyakov VI, Kiro SA, Ennan AA (2013) Formation of primary particles in welding fume. *J Aerosol Sci* 58:9–16

Vishnyakov VI, Kiro SA, Ennan AA (2014a) Bimodal size distribution of primary particles in the plasma of welding fume: coalescence of nuclei. *J Aerosol Sci* 67:13–20

Vishnyakov VI, Kiro SA, Ennan AA (2014b) Multicomponent condensation in the plasma of welding fumes. *J Aerosol Sci* 74:1–10

Vishnyakov VI, Kiro SA, Oprya MV, Ennan AA (2014c) Coagulation of charged particles in self-organizing thermal plasmas of welding fumes. *J Aerosol Sci* 76:138–147

- Vishnyakov VI, Kiro SA, Oprya MV, Ennan AA (2016) Charge distribution of welding fume particles after charging by corona ionizer. *J Aerosol Sci* 94:9–21
- Vishnyakov VI, Kiro SA, Oprya MV, Shvetz OI, Ennan AA (2017a) Nonequilibrium ionization of welding fume plasmas; effect of potassium additional agent on the particle formation. *J Aerosol Sci* 113:178–188
- Vishnyakov VI, Kiro SA, Oprya MV, Ennan AA (2017b) Effects of shielding gas temperature and flow rate on the welding fume particle size distribution. *J Aerosol Sci* 114:55–61
- Yu M, Lin J, Chan T (2008) A new moment method for solving the coagulation equation for particles in Brownian motion. *Aerosol Sci Technol* 42:705–713